Numerical investigation of the seismic response of a UHV composite bypass switch retrofitted with wire rope isolators

Yang Zhenyu[†], Xie Qiang[‡], He Chang[§*] and Xue Songtao[‡]

Department of Civil Engineering, Tongji University, Shanghai 200092, China

Abstract: An ultra-high voltage (UHV) composite bypass switch (BPS) faces increasing seismic challenges when UHV projects extend to high seismic intensity areas. The UHV composite BPS still generates excessive stress at the bottom section although hollow composite insulators with high flexural strength are adopted. Since the standard retrofitting strategy by using stiffer supports cannot reduce stress responses, wire rope isolation is introduced. The optimal design of isolation considers both stress and displacement responses since the slenderness and composite material of insulators contribute to significant displacement. The results show that properly designed isolation can significantly reduce stress without excessive displacement responses. A larger radius configuration helps to improve the applicability of small stiffness isolators under high winds. When the isolation still cannot satisfy the requirement, smaller stiffness isolators with a larger radius, or isolators with increased loops and smaller radius, can be introduced to gain better energy dissipation capacity and effectiveness in response mitigation. Accordingly, a three-step design procedure is proposed to increase the damping force but fix the rotational stiffness of isolation. Hence, the application of wire rope isolation can be extended to UHV composite BPS with a low natural frequency, but conductors with enough redundancy should be used.

Keywords: UHV composite bypass switch; seismic analysis; seismic performance upgrading; wire rope isolator

1 Introduction

In the past decade, several ultra-high voltage (UHV) direct current (DC) transmission networks have been constructed in southwest China to provide the eastern area with clean and cheap power (Zhou *et al*., 2010). However, even though UHV projects can provide cheap and ample electricity, they can also add vulnerability to the power system (Xie and Zhu, 2011).

The bypass switch (BPS), which is fairly new in most converter stations, allows the DC power transmission system to improve system stability and energy usage efficiency. Similar to some circuit breakers, the BPS is a T-shaped post structure and has a large lumped mass on its top, as shown in Fig. 1. In previous seismic events, electrical equipment with a large mass on the top collapsed due to the low strength of brittle ceramic material. For example, as many as 91 circuit breakers failed in the Wenchuan earthquake (Xie and Zhu, 2011).

Recently, many efforts have been made to evaluate the safety and improve the reliability of porcelain equipment under severe seismic inputs. The bottom insulator (Zareei *et al*., 2017) and the metal support (Paolacci *et al*., 2014; Whittaker *et al*., 2007) are found to be the most vulnerable part of post porcelain equipment. Since a flexible supporting frame and joints can significantly amplify the seismic input (Filiatrault *et al*., 2006; Khanmohammadi *et al*., 2018; Li *et al*., 2017a and 2017b), a stiffer support is introduced to improve the seismic performance of 230 kV porcelain transformer bushings (Koliou *et al*., 2013). Similarly, a stiffer supporting structure can also improve the seismic performance of cantilever wall bushings (He *et al*., 2019). However, an inappropriate retrofitting using additional braces may increase the failure probability of a frame structure (Beheshti-Aval *et al*., 2017).

As an alternative to reinforcing the supporting frame, isolation with energy dissipation devices may be a more economical solution due to fewer structural changes (Zhou *et al*., 2018). Several types of base isolation for electrical equipment have been proposed, including friction springs (Riley *et al*., 2006), friction pendulum bearing (Xia *et al*., 2015; Wang *et al*., 2016), wire rope isolator (Alessandri *et al*., 2015; Prost *et al*., 2016), lead alloy isolator (Cheng *et al*., 2018), rubber bearing (Bhagat *et al*., 2017; Chao *et al*., 2017; Zhao *et al*., 2017; Xue *et al*., 2019), polyurethane springs (Gökçe *et al*., 2017), tuned mass dampers (Bai *et al*., 2017), arch-shaped dampers (Lee *et al*., 2018), and pretensioned spring-dampers (Yang *et al*., 2018). As the
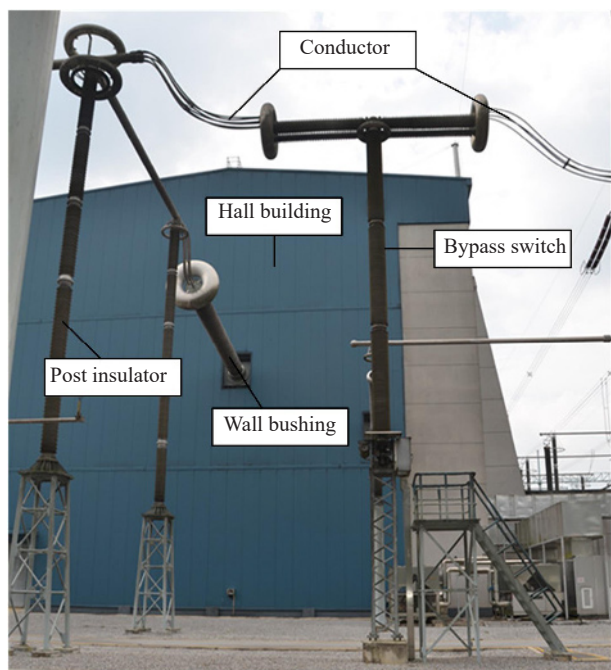
Fig. 1   Picture of an 800 kV BPS in a convert station

hysteresis behavior of dampers is a critical concern, an effective hysteresis model and numerical method have been developed for the analysis of isolated structures (Vaiana *et al*., 2018, 2019a and 2019b).

Currently, the composite insulator has rapidly gained popularity around the world, but it is prone to experience larger displacement than porcelain insulators (Moustafa *et al*., 2016). Moreover, UHV composite insulators have distinctly different physical properties from lower-voltage porcelain ones, including the height, mass, and natural frequency. As a result, the critical part of the equipment and the effectiveness of the retrofitting measures in previous studies need further investigation for UHV composite equipment. Therefore, although wire rope isolation has already been successfully adopted on porcelain circuit breakers and provides excellent effectiveness in stress response mitigation (Alessandri *et al*., 2015; Prost *et al*., 2017), a specific investigation on the applicability of wire rope isolation on slender composite UHV equipment is still necessary. In addition, supplementary viscous dampers can further reduce the displacement of the post equipment (Puff *et al*., 2015; He *et al*., 2018), but also increase the cost by approximately four times (Xie *et al*., 2019). Therefore, a cost-effective solution to the seismic performance upgrading of the slender composite equipment is targeted. Furthermore, as previous studies provide the optimal selection of wire rope isolators by an exhaustive search, this study aims to investigate the critical aspect in the seismic response mitigation and propose a direction for a more effective wire rope isolation design.

Based on an 800 kV composite BPS, a fine FE model was first established. Then, the seismic performance of the BPS was analyzed with 16 input ground motions,

and potential retrofitting measures by adding stiffened plates on a steel supporting frame were discussed. Finally, wire rope isolation was introduced to improve the seismic response of the BPS. The key point in the seismic response mitigation is investigated and a three-step design procedure is proposed.

2 Numerical study of the BPS using FE analysis

2.1 FE model development of the BPS

The 800 kV BPS is composed of two horizontal interrupter units with composite housing, a post insulator comprised of three segments of hollow composite insulators, a metallic box with the controlling unit on the side and a steel supporting frame, as shown in Fig. 2. The three hollow glass fiber reinforced polymer composite insulators, with a total mass of 576 kg, are connected by aluminum flanges, and the bottom insulator rests on two U-steel girders of the metallic box. The weight of the interrupter unit, together with all the components at the top, is 762 kg, while the weight of the support, including the metallic box and supporting frame, is 1,025 kg. The total height of the BPS including the supporting frame is 13.843 m and the gravity center is 9 m above the ground. The latticed steel supporting frame, which is 4 m high, is composed of a steel plate at the top to support the metallic box, four L80 × 8 angle steel columns, and several L40×5 angle braces. The specified mechanical load (SML), under which the insulator fails, of the bottom insulator, is 23.5 kN. The corresponding bending moment at the root section is 66.5 kN·m, which means the ultimate stress of the composite insulator is 84.5 MPa mathematically.

The FE model of the BPS was established using ABAQUS, with the element types and material properties shown in Fig. 3. The insulator is made of composite material with aluminum end fittings, while other parts are generally steel. The four angle steel columns in the supporting frame were modeled by the linear beam element, while the braces, which were connected to steel angles by bolts, were modeled as truss elements that could only bear axial forces. The hollow composite insulator, grading capacitor, aluminum flanges, and metallic box were modeled by the shell element since the geometries of these components were hard to describe by the beam element. The hollow composite insulators and the flanges were connected using an interference fitting and cementation, while other components were connected to each other by bolts. Since composite insulators with aluminum flanges show almost linear elastic behavior before the SML (Epackachi *et al*., 2015), and the stress level of other steel and aluminum components is much smaller than the yield stress, materials are assumed to be in elastic ranges during the analysis. The controlling unit, corona rings and other operating units, were modeled by the nonstructural mass element.

In addition, the conductors were regarded as additional mass elements at the terminal of interruption units. This study does not cover the complicated coupling effect with adjacent apparatuses, as it is assumed that there is enough redundancy in the flexible conductors.

To perform the time history analysis, 16 three-direction ground motion records were selected from the Pacific Earthquake Engineering Research Ground Motion Database and then modulated using SeismoMatch software to improve the matching with the required response spectrum in the Chinese code for seismic design of electrical installations (GB50260-2013).
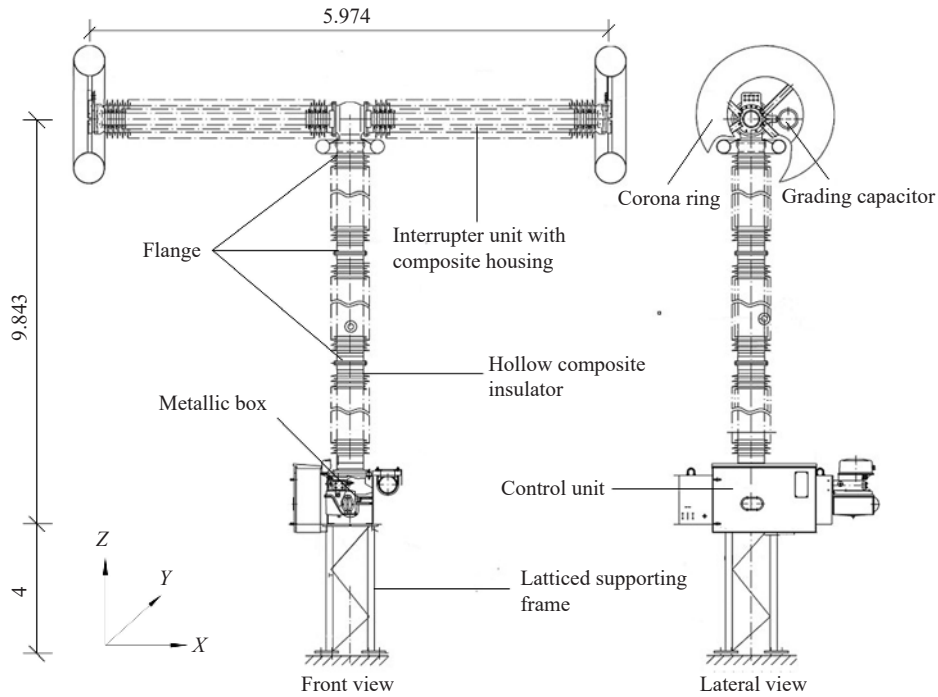

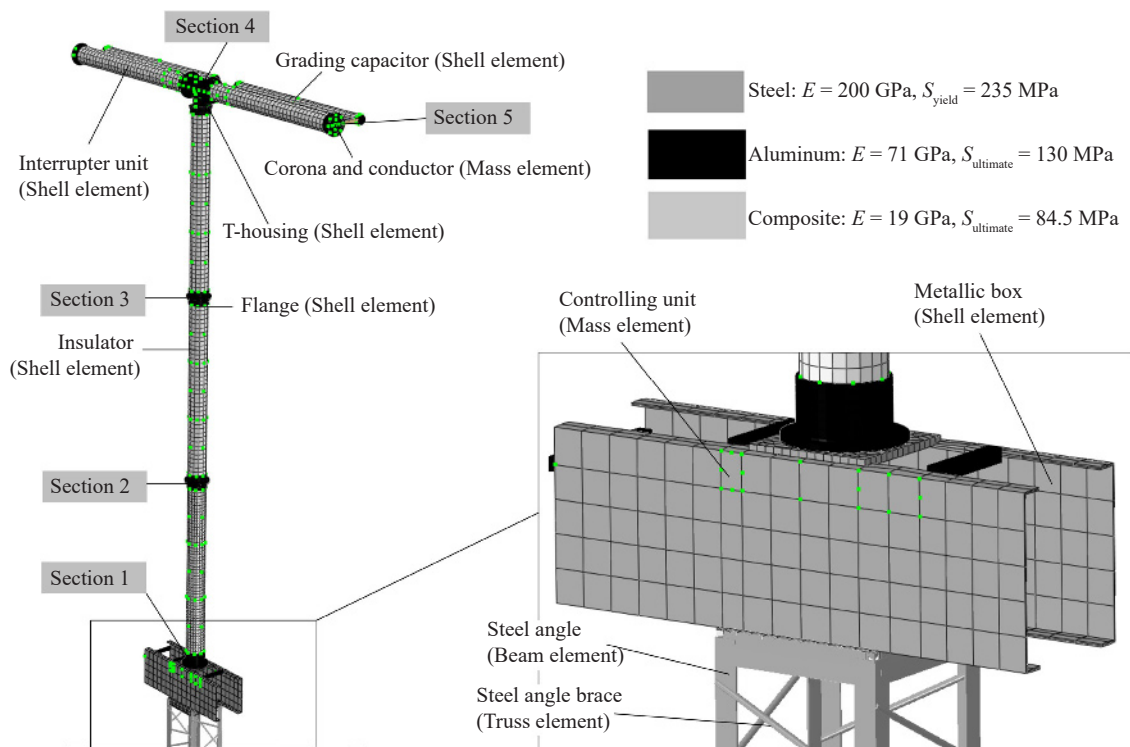**Fig. 2   Components of the 800 kV BPS**

Fig. 3   FE model of the BPS

Particularly, the response spectrum in the range between 1 and 4 s has the largest weight during the modulation, since the characteristic period of the BPS is 2.5 s. As specified in GB50260, the required response spectrum in longitudinal, transverse and vertical directions are 1: 0.85: 0.65, respectively. Table 1 lists the 16 selected records, and Fig. 4 shows the response spectra of the modulated records, the mean spectrum, and the target spectrum from GB50260. In addition, as the modulation aims at improving the response spectrum match, peak ground acceleration (PGA) of the modulated records varies.

2.2 Seismic analysis of the BPS

Modal analysis was first performed to offer brief insights into the dynamic property of the BPS. Table 2 lists the eigenfrequencies and corresponding accumulated modal effective mass ratio of the first five modes and the 16th mode, in which the accumulated modal effective mass reaches over 90% of the total mass. Since the BPS is quite slender and is composed of low-stiffness composite insulators, the natural frequency of the BPS is only 0.390 Hz. In addition, the high-order modes contribute significantly to the effective mass and

Table 1 List of 16 modulated and two unscaled earthquake records

| Record No.	Earthquake name	Station	Year	Magnitude	Original PGA (g)	Modulated PGA (g)
RSN6	Imperial Valley	El Centro	1940	6.95	0.23	0.37
RSN15	Kern County	Taft	1952	7.36	0.16	0.42
RSN125	Friul	Tolmezzo	1976	6.5	0.32	0.51
RSN139	Tabas	Dayhook	1978	7.35	0.33	0.47
RSN639	Whittier Narrows	Obregon	1987	5.99	0.41	0.53
RSN848	Landers	Coolwater	1992	7.28	0.35	0.42
RSN1045	Northridge	Newhall	1994	6.69	0.36	0.57
RSN1101	Kobe	Amagasaki	1995	6.9	0.31	0.40
RSN1158	Kocaeli	Duzce	1999	7.51	0.32	0.45
RSN1504	Chi-Chi	TCU067	1999	7.62	0.42	0.41
RSN1787	Hector Mine	Hector	1999	7.13	0.31	0.47
RSN3548	Loma Prieta	Los Gatos	1989	6.93	0.44	0.65
RSN3965	Tottori	TTR008	2000	6.61	0.39	0.56
RSN4031	San Simeon	Templeton	2003	6.52	0.43	0.53
RSN4800	Wenchuan	Zengjia	2008	7.9	0.42	0.40
RSN4896	Chuetsu-oki	Kashiwazaki	2007	6.8	0.39	0.37
RSN811	Loma Prieta	WAHO	1989	6.93	0.54	/
RSN3475	Chi-Chi	TCU080	1999	6.30	0.55	/
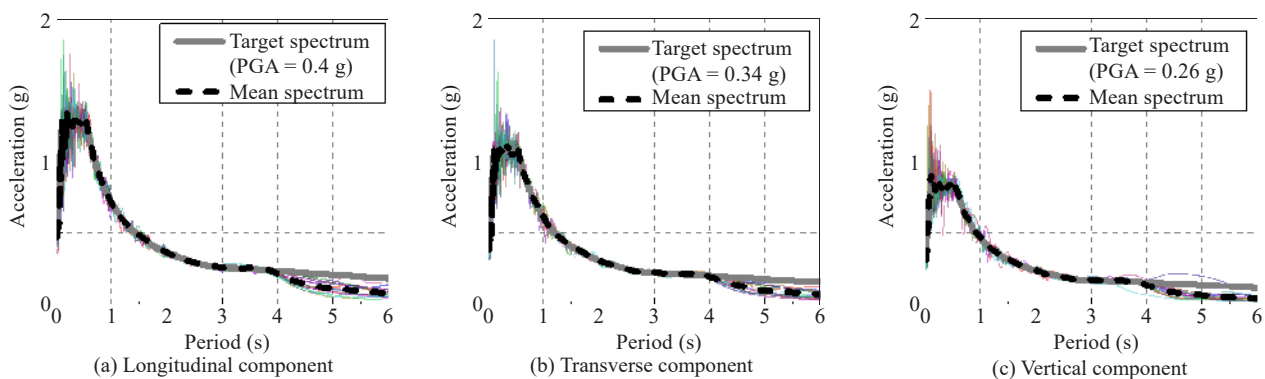
Fig. 4 Response spectra of the 16 modulated records in three directions (2% damping, $T_g = 0.55$ s)

the deformation of post insulators, as shown in Fig. 5, in which the shadow and solid shapes are the normal shapes and the deformed shapes, respectively.

A linear modal dynamic time history analysis was performed using the 16 scaled records. The first 100 modes were included in the analysis to achieve over 90% of the accumulated modal effective mass in all directions. The damping ratio of composite insulators varies in different studies, ranging from 0.84% to 2.5% (Epackachi *et al*., 2015; Li *et al*., 2018; Roh *et al*., 2012). However, since the UHV equipment assembled by several composite insulators has a larger damping ratio

up to 2.5% (Li *et al*., 2018), the damping ratio for BPS is set to be 2% approximately since the BPS is composed of five insulators. In order to fully verify the seismic performance of BPS, the longitudinal component, which is modulated following the 100% standard response spectrum, will excite the BPS in *X* and *Y* direction in turns, with the transverse component in the other direction, as listed in Table 3.

Table 4 shows the average values of the peak responses of the BPS, including relative displacement, absolute acceleration, and stress under the 16 pairs of records at the five sections, whose positions are shown
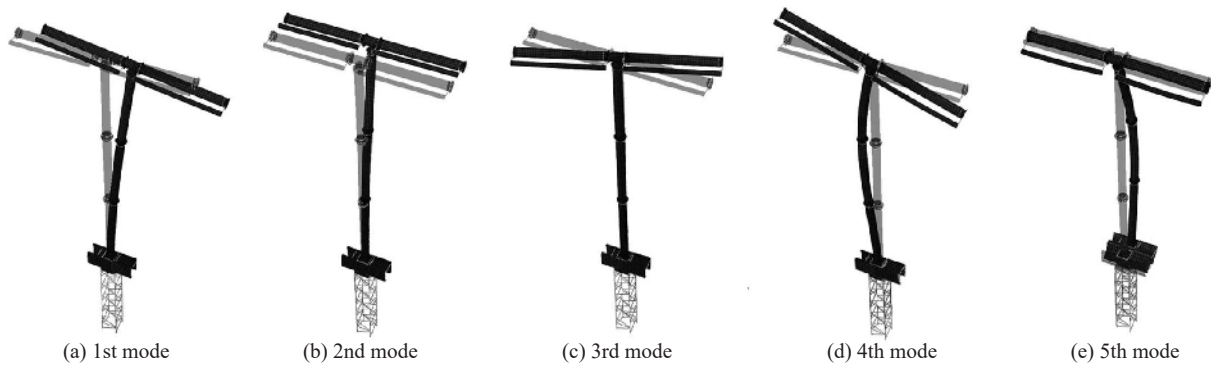
| (a) 1st mode | (b) 2nd mode | (c) 3rd mode | (d) 4th mode | (e) 5th mode |

Fig. 5   First five mode shapes of the BPS

Table 2   Eigenfrequencies and accumulated modal effective mass ratios of selected modes

Mode No.	Eigenfrequency (Hz)	Accumulated modal effective mass ratio			
		X	*Y*	*X* rotation	*Y* rotation
1	0.390	0.432	0.000	0.000	0.873
2	0.418	0.432	0.458	0.888	0.873
4	2.60	0.520	0.458	0.888	0.914
5	3.67	0.520	0.751	0.975	0.919
16	15.9	0.922	0.942	0.999	0.998

Table 3   Seismic input for two cases

Direction	*X*	*Y*	*Z*
Case 1	Longitudinal component	Transverse component	Vertical component
Case 2	Transverse component	Longitudinal component	Vertical component

Table 4   Mean value of peak responses of 16 modulated records under two input modes

Section	Case 1			Case 2		
	Acceleration (m/s²)	Displacement (m)	Stress (MPa)	Acceleration (m/s²)	Displacement (m)	Stress (MPa)
1	9.8	0.020	46.1	11.0	0.024	47.0
2	14.4	0.109	38.9	15.3	0.108	40.2
3	15.2	0.288	23.8	16.7	0.285	23.8
4	6.7	0.538	7.9	7.2	0.541	7.6
5	14.4	0.596	/	14.4	0.571	/

in Fig. 3. The maximum stress of composite material, aluminum and steel support under the 16 records are 56.8, 71.6 and 160.9 MPa, respectively, which are smaller than the ultimate stress in Fig. 3. In addition to the ground motion, other loads should also be included in the stress safety factor estimation of the BPS. According to GB50260, the total stress response S_{total} considering all load effects can be calculated by:

$$S_{total} = S_e + 0.25 \times S_w + S_t + S_p + S_G \qquad (1)$$

where S_e, S_w, S_t, S_p and S_G are the stresses caused by the earthquake, design wind load, terminal load, inner pressure and gravity, respectively. Although Eq.(1) was originally used in the experimental qualification in GB50260, it is still introduced here due to its ease in handling the load combination.

The stress safety factor n_s, which should be larger than 1.67 as specified by the user, is calculated as:

$$n_s = S_{limit} / S_{total} \qquad (2)$$

where S_{limit} is the ultimate stress of the concerned component and derived from the SML. The wind-induced stress, S_w, is calculated following the load code for the design of building structures (GB50009-2012). The wind speed is 30 m/s, while distributed wind loads and the wind vibration factor are adopted as the BPS is quite slender. The total wind load is 4.96 and 5.37 kN in the X and Y direction, respectively, so S_w reaches 50.82 MPa at the root section of the post insulator. This is surprisingly even larger than the stress caused by the earthquake, because the BPS is too flexible and tall. Since the conductors are modeled as the additional mass on the model and gravity is already applied before the seismic events, S_t and S_G are already included in S_e. The stress from inner pressure, S_p, is 2.5 MPa in the longitudinal direction of the composite tube, according to the working pressure 0.6 MPa. Therefore, the total stress can be expressed as $S_{total} = 47.0 + 0.25 \times 50.82 + 2.5 = 62.2$ MPa while the ultimate stress, S_{limit}, is 84.5 MPa; thus, the stress safety factor $n_s = 84.5 / 62.2 = 1.36$, which is smaller than the required value of 1.67.

2.3 Critical section of the slender insulator

The BPS generates significant vibration at middle sections of post composite insulators during seismic events. Section 3 generates the maximum acceleration in all seismic events, which shows the influence of high order vibration modes. Figure 6 (a) shows the power spectral density of the acceleration response in the Y direction at Section 4 and Section 3 under the seismic record RSN1504. The higher order modes, namely the 5th mode in Table 2, dominates the acceleration at Section 3. On the contrary, the acceleration response at Section 4 is mainly low frequency components around the natural frequency of 0.418 Hz. Different from the acceleration response, the displacement response at Section 4 is larger than that at Section 3, as the displacement is still dominated by low frequency components, as shown in Fig. 6(b).

The influence of high-order modes casts doubt on the maximum stress position of the post insulator. Figure 7 shows the target response spectrum of GB50260, while the vertical solid lines represent the eigenfrequencies of the 2nd and 8th modes. According to the required spectrum, a high-frequency structure (natural frequency from 1.8 to 10 Hz) is more likely to suffer a larger inertia load than a low-frequency one (natural frequency below 1.8 Hz). Therefore, it is supposed that the 8th mode still has the possibility of dominating the stress response.

Following the modal decomposition method, the bending moment at the section with a height of h_0 above the root section can be written as:

$$M_b(h) = \{h - h_0\}^T \boldsymbol{Ku} = \sum_i \{h - h_0\}^T \boldsymbol{M\phi_i}\ddot{Y}_i = M_{ri}\ddot{Y}_i \quad (3)$$

where M_{ri} is the modal effective mass in the rotational X or Y direction at height h_0. Note that the relative height $(h - h_0)$ will be zero if the section height is smaller than h_0. Table 5 lists the modal parameters, including M_{ri} of seven modes at three sections in the Y direction. Generally, M_{ri} of the first mode at the root section is larger than those of higher modes at other sections. However, it is much more difficult, although not impossible, for high order modes to dominate the stress response of a slender composite insulator.
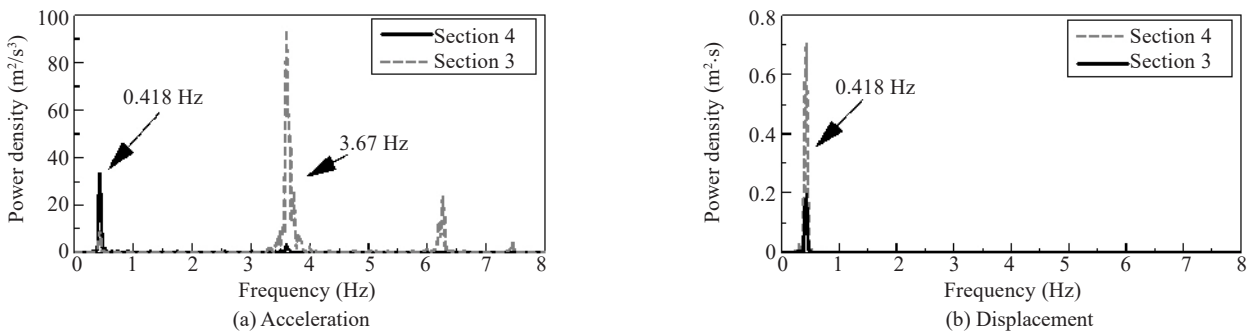

(a) Acceleration

(b) Displacement

Fig. 6 Acceleration and displacement power density of sections 3 and 4 under RSN 1504 in the Y direction

Only in some specific conditions can the maximum stress occur at the middle sections. For example, some seismic records in stony soil generate very large acceleration responses in high frequency ranges, such as RSN811 and RSN3474, as shown in Fig. 7. On the contrary, the low frequency responses are quite small under these records. For porcelain low voltage electrical equipment, whose natural frequency is generally larger than 2 Hz, the acceleration response of high-order modes will not significantly surpass that of the first order mode as the spectral response of the first mode is already relatively large. However, for UHV composite equipment, whose natural frequency is always lower than 1 Hz, the eigenfrequency of a high order mode may locate approximately to the predominant period of the site, which can result in failures at middle sections.
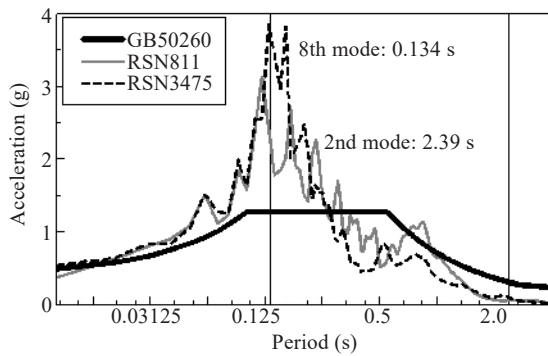

Fig. 7 Spectral responses of selected modes on the required response spectrum in the code and the response spectrum of selected records

Table 6 shows the peak stress at three sections in Fig. 3 under the two unscaled natural records. Middle sections undergo larger stresses than the root section under RSN811 and RSN3475 in two directions. Thus, an additional validation of the middle section stress will be necessary when the seismic input contains ample high-frequency components. However, for an input that is compatible with a target response spectrum, this phenomenon rarely occurs. Therefore, it is suggested that in a normal design of composite equipment following codes, the root section is still regarded as the critical section.

2.4 Displacement consideration of BPS

Since the BPS is quite high and slender, the seismic event, as well as wind loads, can lead to significant displacement at the top. As listed in Table 4, the seismic event can result in displacement approximately 0.6 m in either the X or Y direction. Moreover, the wind load, with a wind velocity of 30 m/s, results in a displacement of 0.29 and 0.7 m in X and Y direction, respectively. For the T-shape BPS, the projection area in the X direction is far smaller than that in the Y direction. However, considering the layout of the BPS and adjacent equipment, the displacement resulting from seismic events is more critical.

As shown in Fig. 8, the displacement in the Y direction, namely the out of plane deformation, cannot lead to significant deformation of the conductors. For example, the displacement of 0.7 m in Y direction only results in 0.11 m deformation of the conductor. However,

Table 5   Modal parameters of the selected seven modes

Mode order	f_i (Hz)	M_{ri} (kg·m)		
		Section 1	Section 2	Section 3
2	0.42	8029.7	5177.3	2441.0
5	3.60	357.1	-222.4	-297.5
7	6.24	-447.2	-164.2	36.8
8	7.45	-34.2	-223.6	-269.9
10	10.67	-15.0	38.7	-22.1
11	11.11	69.6	-13.6	-39.1
16	16.08	-64.5	-9.7	-48.9

Table 6 Peak stresses at three sections under two unscaled natural records

Section	Longitudinal component in X (MPa)		Longitudinal component in Y (MPa)	
	RSN811	RSN3475	RSN811	RSN3475
1	13.5	13.4	15.4	16.4
2	14.9	11.7	14.5	12.6
3	15.0	11.0	12.7	17.1
4	20.9	16.1	19.9	10.2

a displacement over 0.5 m in the *X* direction can severely challenge the deformability of conductors. As a result, the 0.596 m displacement during seismic events requires larger redundancy of conductors than that resulting from wind loads. Therefore, during the qualification of the UHV composite BPS, the stress safety factor should be verified under seismic events and wind loads in the *Y* direction, while the displacement response should be checked in the *X* direction.

In summary, since the safety factor of the BPS cannot satisfy the requirement and the displacement at the top is quite large, the key point of the seismic upgrading is reducing the stress at the root section without generating excessive displacement at the top.

3 Seismic performance retrofitting of the BPS

3.1 Layout and modeling of the isolation

Since the stress at the root section of the post insulator exceeds the limit, seismic performance retrofitting of the BPS is necessary. For some HV porcelain equipment, a stiffer support can help to reduce the seismic input on the equipment, since a flexible steel supporting frame can greatly amplify the ground input. As shown in Fig. 9, the increase in the frequency of some HV porcelain equipment results in a decrease of inertial loads on the equipment, if the seismic input is compatible with the required spectrum. However, for UHV composite BPS, whose natural frequency is only 0.39 Hz, a stiffer support that increases the frequency can also increase the inertial load. Consequently, reinforcement on the steel support cannot improve the stress safety factor of the composite BPS. Alternatively, isolation consisting of wire rope isolators (WRI), which has been widely used for HV porcelain equipment including circuit breakers and disconnect switches, is introduced and specifically designed for the slender UHV composite BPS.

The WRI with hysteresis behavior not only reduces the natural frequency of the BPS but also provides considerable damping force that can further help to dissipate seismic inputs. Since the composite insulator has high flexural strength but is quite slender, the displacement response, rather than the stress, may be the critical concern during the design.

Considering the biaxial seismic inputs in the horizontal directions, there are typically a total of four WRIs at the bottom of a single BPS, as shown in Fig. 10(a). The BPS is mounted on the steel octagonal plate using bolts while the octagonal plate is supported by WRIs. The mounting plate acts as the connection between the WRI and the foundation. In engineering practice, a reinforced concrete foundation is preferred to provide a reliable base for the isolated BPS.

The FE model of the fixed base BPS was updated to include the isolation. The mounting plate was modeled by the beam element, which provided a convenient connection to the adjacent one-dimensional elements. A three-dimensional user-defined element (UEL), which
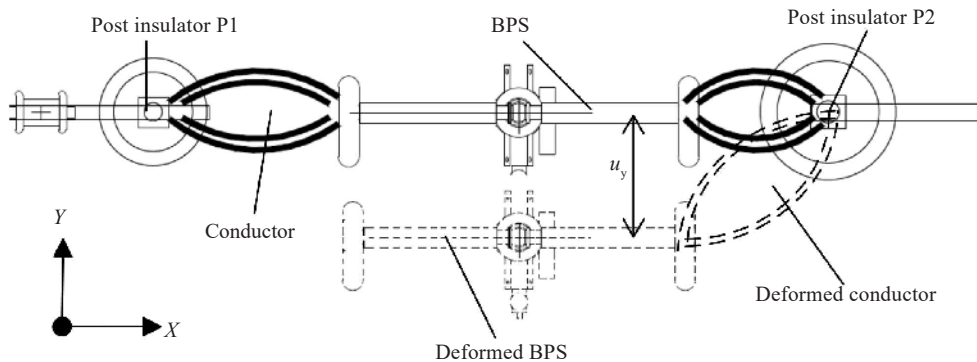

Fig. 8   Overhead view of the BPS and adjacent equipment

(a) Low voltage porcelain equipment   (b) Some UHV composite equipment
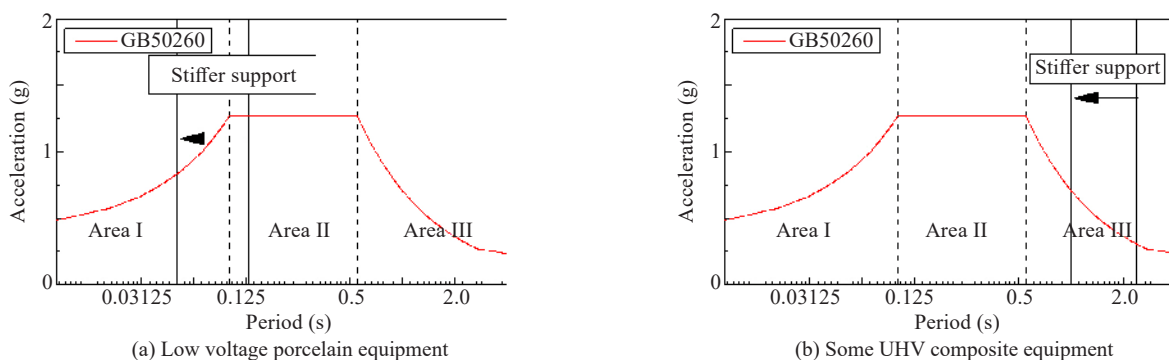
Fig. 9   Influence of a stiffer support on the response spectrum of GB50260

is a one of a kind ABAQUS subroutine that can define an element with designated mechanical behaviors, was employed to model the wire rope. The UEL can be regarded as three nonlinear springs in X, Y, and Z direction that provide reaction forces in each step following specified hysteresis behavior, as shown in Fig. 10(b).

WRIs show evident nonlinearity in the shear, roll, and compression-tension (C-T) directions, which has been studied for decades (Tinker and Cutchins, 1992; Wang *et al*., 2015; Vaiana *et al*., 2017). The Bouc-Wen model was widely used in the modeling of a wire rope device (Schwanen *et al*., 2004). Since wire rope shows asymmetric behavior in the compression-tension direction, a polynomial exponent was adopted to describe the hysteresis curve of the wire rope device in compression (Demetriades, 1993). In addition, the asymmetry can also be simulated by using different hysteresis parameters in compression and tension (Ni *et al*., 1999).

However, as the total weight of the 800 kV BPS with the isolation is approximately 3.5 t, the static load capacity of a single wire rope device in the C-T direction should be larger than 8.5 kN. Therefore, three candidate wire rope devices, WR28-400, WR36-200, and WR40-200 with sequentially increased stiffness, are introduced to achieve an acceptable solution to the seismic performance retrofitting of the BPS. Among the candidate isolators that satisfy the vertical bearing capacity requirement, WR28-400 and WR40-200 have the smallest and largest stiffness, respectively. Since the effectiveness of WRI is primarily from the axial deformability and the slender BPS is elongated by the rocking motion, the nonlinearity in shear and roll direction is ignored during the analysis. The horizontal stiffness of WRI is set to be the vibration stiffness specified in the product brochure (ITT Enidine). Meanwhile, the hysteresis effect in the horizontal directions are still suggested to be included when hysteresis parameters are available, as newly developed models can help to improve the accuracy of the analysis (Vaiana *et al*., 2018 and 2019).

Figure 11 (c) shows the hysteresis curves of WR28-400 and WR36-200 (Paolacci *et al*., 2008), and the experimental hysteresis curve of the WR40-200 is provided by the manufacturer to perform the analysis. The wire rope device is subject to linear increasing displacement loading during the cycling test with a loading frequency of 0.5 Hz.

The general constitutive equation of the Bouc-Wen model is:

$$F(t) = f_1(u(t)) + f_2(z(t)) \tag{4}$$

where f_1 and f_2 are functions of displacement, F is the WRI axial restoring force, while u and z are device axial displacement and hysteretic variable, respectively, which can be written as:

$$\dot{z} = \left\{A - \left[\beta \mathrm{sign}(z \cdot \dot{u}) + \gamma\right] \cdot |z|^n\right\}\dot{u} \tag{5}$$

where A, β, γ, and n are hysteresis parameters. Generally, f_1 and f_2 are linear equations, so the restoring force F can be decomposed into an elastic and a hysteretic part as:

$$F(t) = k_\mathrm{e}u(t) + k_\mathrm{i}z(t) \tag{6}$$

where k_e and k_i are stiffness parameters. However, as shown in Fig. 11(b), the hysteresis curve in the C-T direction shows stiffness hardening and softening in tension and compression, respectively. Therefore, a simplified exponent of the polynomial (Paolacci *et al*., 2008) is a convenient way to describe the asymmetric behavior in the compression-tension direction, so Eq. (4) can be expressed as:

$$F(t) = k_\mathrm{e}\left(\exp(b_1 u(t)) + \exp(-b_2 u(t))\right) + k_\mathrm{i}z(t)\exp(\alpha u(t)) \tag{7}$$

However, symmetric hysteresis parameters in loading and unloading cannot achieve satisfactory coincidence between the experimental and numerical curve
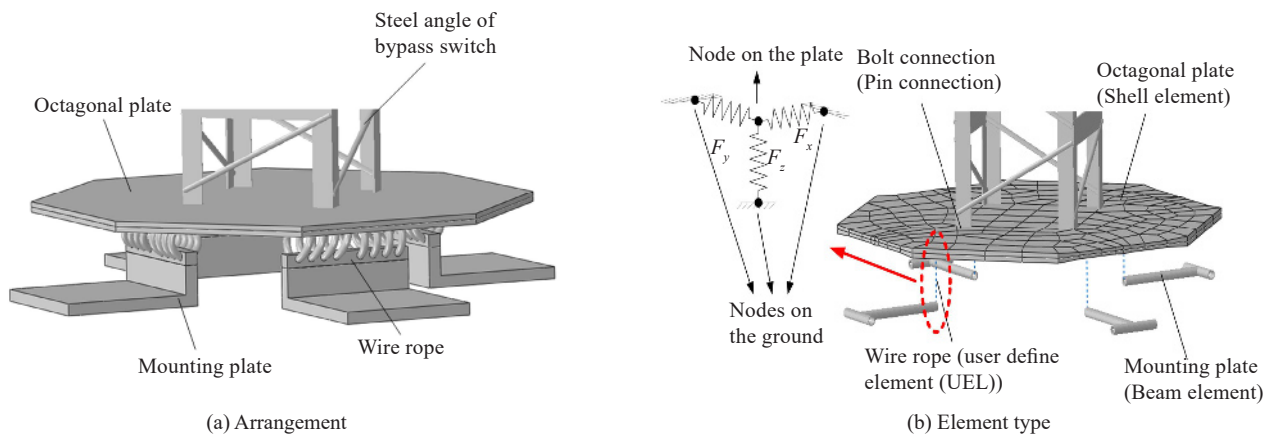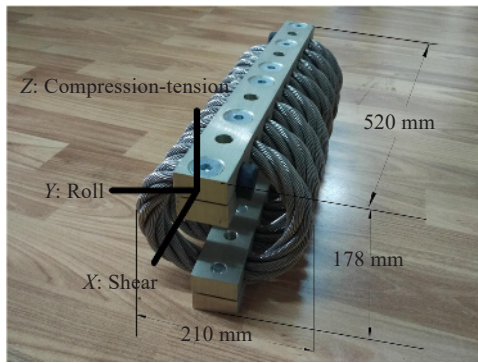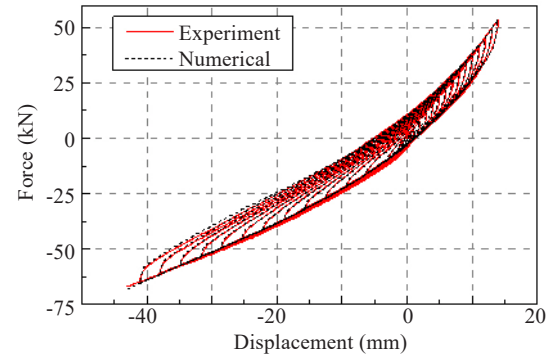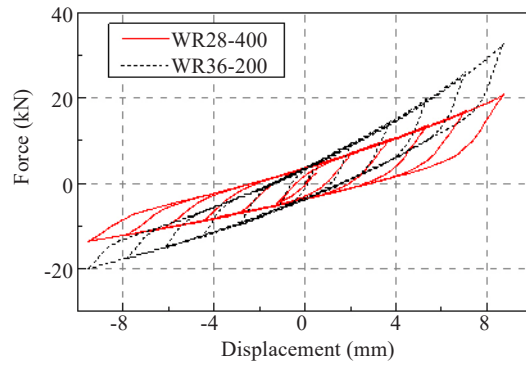

(a) Arrangement   (b) Element type

Fig. 10 Arrangement and element type of the isolation FE model

(a) Dimension of WR40 isolator

(b) Hysteresis curve of WR40 in C-T direction

(c) Hysteresis curve of WR28 and WR36 in C-T direction

Fig. 11   Dimension of WR40-200 and hysteresis curve of three wire rope devices

in Fig. 11, so different hysteresis parameters, including A, β and γ, in loading and unloading are introduced:

$$\dot{z} = \begin{cases} \left\{ A_1 - \left[\beta_1 sign(z \cdot \dot{u}) + \gamma_1 \right] \cdot |z|^n \right\} \dot{u} & \dot{u} > 0 \\ \left\{ A_2 - \left[\beta_2 sign(z \cdot \dot{u}) + \gamma_2 \right] \cdot |z|^n \right\} \dot{u} & \dot{u} < 0 \end{cases} \quad (8)$$

Therefore, the restoring force of the WRI can be obtained using Eqs. (7) and (8). The hysteresis parameters of the modified Bouc-Wen model are identified by the Levenberg-Marquardt algorithm. The Levenberg-Marquardt algorithm combines the advantages of both the Gauss-Newton algorithm and Gradient descent method by introducing a damping coefficient λ, which is set to be 0.02 in the initial step in this fitting. With the identified parameters in Table 7, the modified Bouc-Wen model can accurately reproduce the hysteresis curve, especially when the displacement is large, as shown in Fig. 11(b).

Step-by-step time history analysis is necessary for the numerical analysis of the isolated BPS due to the nonlinearity in WRIs. Damping of the BPS in the time history is implemented using the Rayleigh damping matrix by specifying the damping ratio at two frequencies. As the influence of high order modes is not negligible in the composite BPS, four vibration modes are included in the estimation of Rayleigh damping coefficients. The 3rd mode is not included because the torsional movement has

little influence on the response. Taking the 1st, 2nd, 4th, and 5th modes into consideration, the Rayleigh damping coefficients are obtained by fixing the damping ratio at 0.02 for frequencies of 0.397 and 3.058 Hz to achieve damping ratio approximate to 0.02 at the four modes. The actual damping ratio of the four modes is 0.0208, 0.0192, 0.0176 and 0.0226, respectively. Although the actual damping ratio of higher modes is larger than 0.02, the deviation in the damping ratio will not affect the responses of the first five modes, especially the first two modes, which dominate the seismic responses.

3.2 Design of isolation considering stress and displacement responses

The selection and layout of the WRI will affect the effectiveness of the wire rope isolation, so an optimal design is demanded to improve the seismic performance of the isolated BPS. As shown in Fig. 12(b), the rotational stiffness of the isolation can be adjusted by changing WRI types and varying the radius r, which is the distance from the rotational center of the plate to the WRI. In Fig. 12, the dashed rectangle represents the outline of the wire rope while the solid line rectangle inside represents the mounting beam. Considering the dimension of the octagonal plate and the WRI, r is proposed to be no smaller than 489 mm. Therefore, r is set to be 489 mm, 555 mm, 655 mm, 755 mm and 855 mm during the optimization. Since the estimation of conductor redundancy and stress safety factor relies on

the displacement in the X and Y directions, respectively, the effectiveness of isolation for displacement and stress response will be verified in Case 1 and Case 2 accordingly. Notably, the deformation of conductors under seismic inputs should not be much larger than that generated by wind loads to achieve a minimum required conductor redundancy. Meanwhile, as specified in previous sections, the allowable stress resulting from seismic inputs should be smaller than 35.4 MPa, with which the stress safety factor is exactly 1.67 according to Eqs. (1) and (2).

According to the designer of the convert station, there will be problems in the design of conductors when the displacement exceeds 0.7 m. Thus, the optimization is performed using the 16 seismic inputs in Case 1 and Case 2 by minimizing the stress response while the displacement keeps below 0.7 m under seismic inputs and wind loads. Figure 13 shows the peak stress and displacement responses of the isolated BPS with WR28 and various radii r under RSN6, RSN1504, which are the most critical inputs. Although most configurations using WR28 can significantly mitigate the stress response to allowable values, the displacement response satisfies the requirement only when r is 855 mm. Therefore, isolation

with four WR28 devices with the radius r of 855 mm is selected accordingly. Figure 14 compares the peak stress and the conductor deformation of the isolated and fixed base BPS under 16 seismic inputs. The average stress decreases from 47.0 MPa to 23.3 MPa after the employment of the base isolation and the average stress safety factor reaches 2.19, which is larger than the required value of 1.67.

As shown in Fig. 14, the maximum deformation of conductors during seismic events is smaller than the requirement of 0.7 m. The wind induced displacement decreases sharply with the increase of radius r for isolation with WR28 isolators, so a larger radius is effective when a WRI with small stiffness is employed. In addition, since the conductors are regarded as a soft connection to adjacent equipment, the total length of the conductors should be larger than the distance between edges of the conductors. Therefore, according to Fig. 14, the conductor curve should be able to stretch or shorten 0.7 m without causing considerable force on the BPS.

As shown in Fig. 15, a smaller radius r, which contributes a smaller rotational stiffness of the isolation, leads to a decrease in stress but an increase in displacement. However, the effectiveness of the isolation not only relies

Table 7 Hysteresis parameters of the modified Bouc-Wen model in compression-tension directions

Status	A	β	γ	n	k_e (N/m)	b_1	b_2	k_i (N/m)	α
Loading	5.03×10^{-3}	4.31×10^3	-4.18×10^3	1.09	3.39×10^4	53.3	15.8	1.24×10^8	-11.03
Unloading	8.98×10^{-3}	2.68×10^3	-1.57×10^3						

(a) Range of allowable r

(b) Definition of r and d
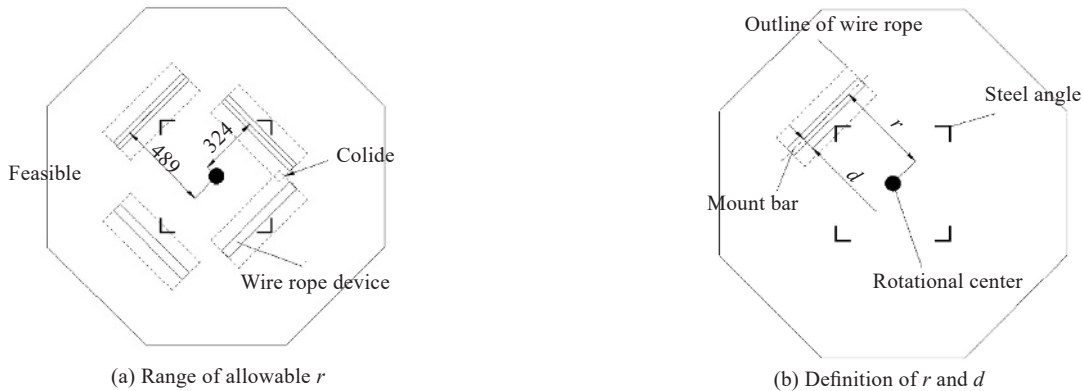
Fig. 12 Layout of the octagonal plate (unit: mm)

(a) Stress
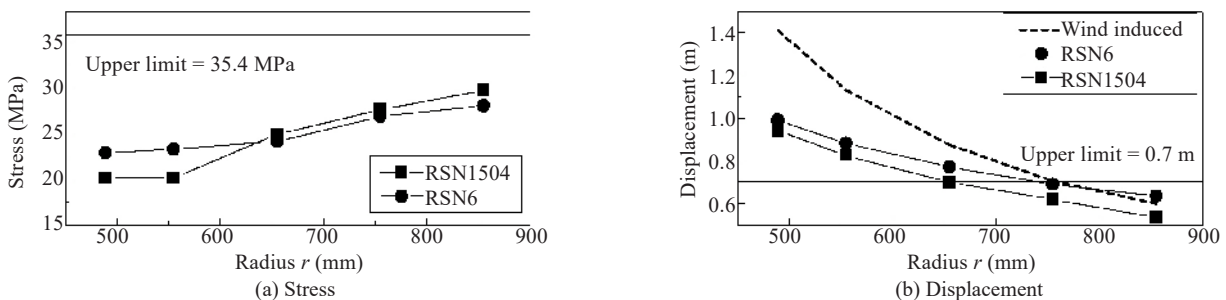
(b) Displacement

Fig. 13 Peak stress and displacement responses for WR28 under various r and seismic inputs

(a) Maximum stress at the root section

(b) Maximum deformation of conductors
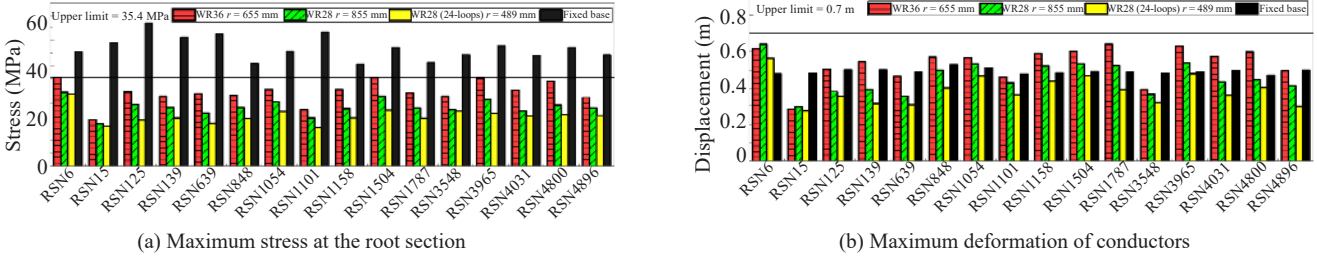
Fig. 14 Peak responses of isolated and fixed base BPS

(a) Stress

(b) Displacement

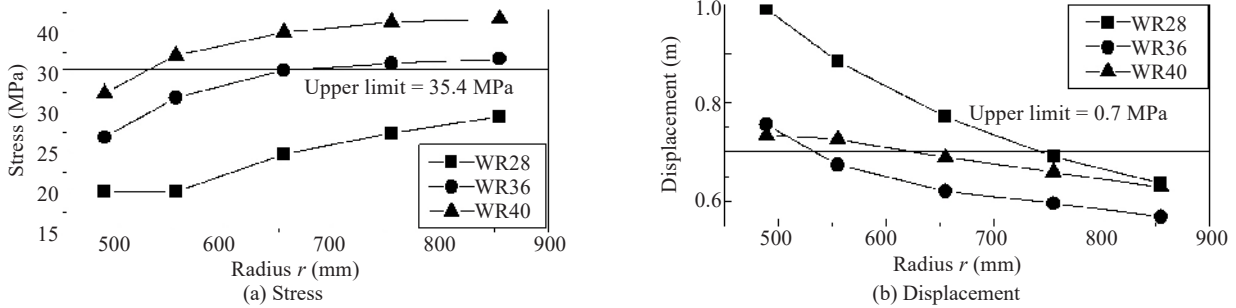**Fig. 15   Peak stress and displacement responses for different wire rope devices with various radius *r* under RSN6**
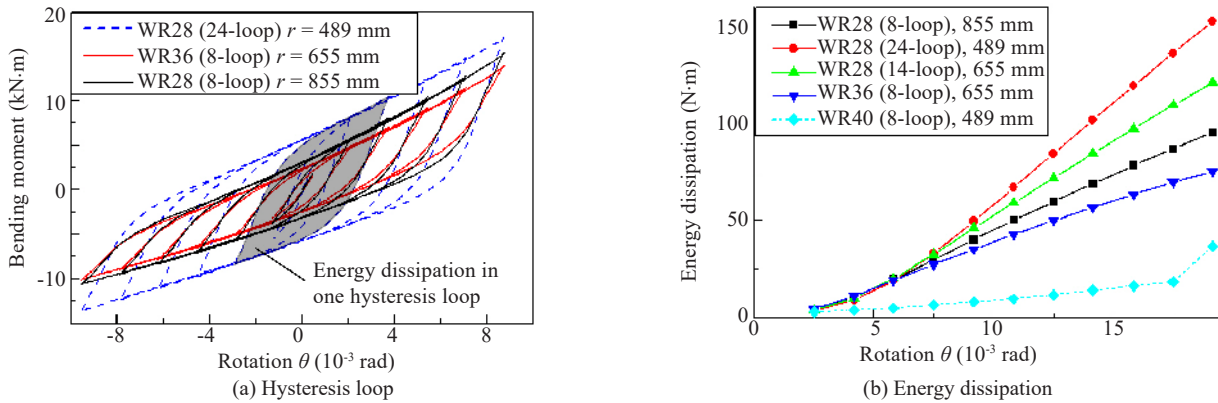

(a) Hysteresis loop

(b) Energy dissipation

Fig. 16   Energy dissipation by a single wire rope device in different configurations

on the rotational stiffness but also depends on the energy dissipation capacity of the WRI. As shown in Fig. 16, WR28 device with a radius of 855 mm (Configuration 1) leads to almost the same rotational stiffness but a larger hysteresis loop than WR36 isolator with a radius of 655 mm (Configuration 2). However, Configuration 1 results in smaller stress as well as displacement response than Configuration 2 under most seismic inputs, as shown in Fig. 14. In addition, WR28 isolator with a smaller radius, for example, when *r* is only 655 mm, can also result in satisfactory stress response but will lead to excessive displacement. Therefore, it is suggested to adopt a WRI with smaller stiffness and larger radius *r* following the rotational stiffness equivalent replacement, when the current configuration is not effective enough.

Furthermore, as the increase in energy dissipation capacity is the critical parameter that reduces the seismic responses, rotational stiffness equivalent replacement using the same series WRI with increased loops and smaller radius *r* is proposed. Typically, WRI is an

8-loop device, as shown in Fig. 11(a). According to the manufacturer, the number of loops can be adjusted if necessary. Therefore, the 24-loop WR28 isolator with radius *r* of 489 mm has a significantly larger hysteresis loop than the 8-loop WR28 isolator with radius *r* of 855 mm, as shown in Fig. 16(a). In addition, when fixing the rotational stiffness, a smaller radius *r* with more wire rope loops is more effective in energy dissipation, as shown as the solid lines in Fig. 16(b). On the contrary, the insufficient effectiveness of the WR40 can be explained by the poor energy dissipation capacity.

The larger hysteresis loop in Fig. 16 can be explained by the yield of WRI. Provided an *m*-loop and *n*-loop WRI with radius D_m and D_n, respectively, the stiffness equivalent replacement is based on the initial stiffness of the isolator by assuming the restoring force of each loop follows Eq. (6):

$$k_{\text{rotation}} = m\left(k_{\text{e}} + k_{\text{i}}\right)D_m^2 = n\left(k_{\text{e}} + k_{\text{i}}\right)D_n^2 \qquad (9)$$
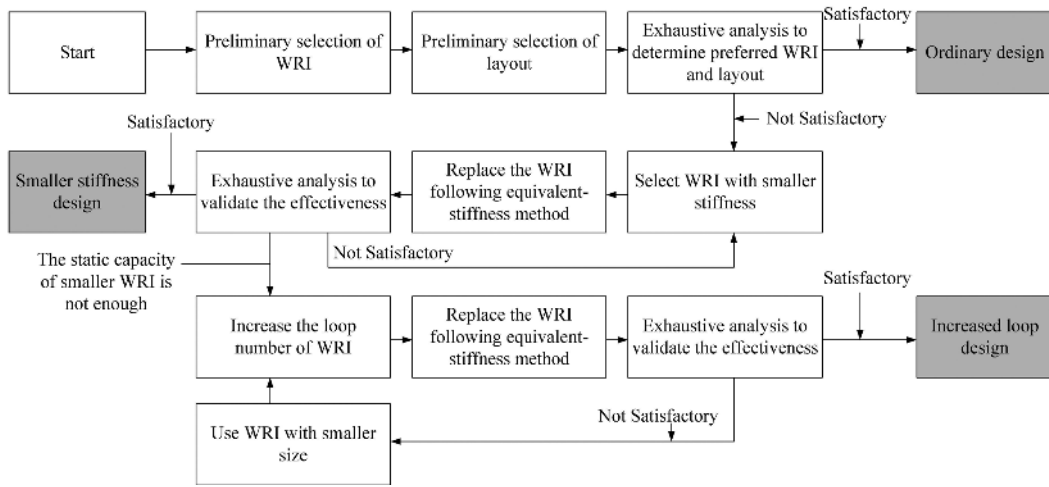
Fig. 17   Design procedure of the wire rope isolation for composite post equipment
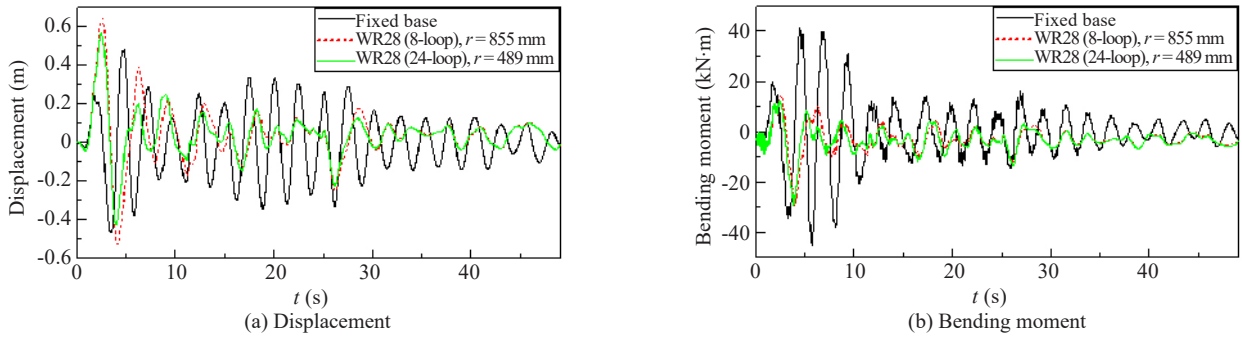

(a) Displacement

(b) Bending moment

Fig. 18   Seismic response time history of the fixed base and isolated BPS

However, as z will keep at z_{max} after the WRI yields, it is easy to estimate the energy dissipation E when the rotation is θ:

$$E_m = \theta m k_i z_{max} D_m = \frac{D_n}{D_m} \theta n k_i z_{max} D_n = \frac{D_n}{D_m} E_n \qquad (10)$$

Equation (10) predicts that a smaller radius r is preferred when the WRI increases its loop number, which coincides with Fig. 16(b). Therefore, a specially designed WRI with increased loops can provide more energy dissipation during the stiffness equivalent replacement. As shown in Fig. 14, the increased loop WR28 increases the stress safety factor to 2.41 and further reduce the displacement response.

However, a special design and manufacture of an increased loop WRI are expensive and time-consuming, so ready-made types of WRI are still preferred. Therefore, a three-step design procedure of the wire rope isolation for composite equipment is proposed, as shown in Fig. 17. In the ordinary design step, WRI and corresponding layout are initially selected following the vertical bearing capacity and exhaustive analysis. If the recent design is not satisfactory, smaller stiffness WRI with larger radius r can be introduced following stiffness equivalent replacement to obtain a smaller stiffness design. When the first two designs are not effective enough, WRI with increased loops can be introduced to further increase the energy dissipation capacity, which is called increased loop design. Taking the isolation for the BPS as an example, the first two steps result in the 8-loop WR28 isolator with radius r of 855 mm, while the increased loop design will lead to 24-loop WR28 isolator with r of 489 mm. As shown in Fig. 18, both of the configurations using WR28 can significantly reduce stress while preventing excessive displacement response at the top.

4   Conclusion

The seismic analysis concludes that the BPS without any retrofitting cannot satisfy the safety factor requirement. The modal effective mass at various heights predicts that the maximum stress will appear at the root section, except in situations where the high frequency responses are much larger than the low frequency responses. In addition, the ordinary retrofitting by using a stiffer steel supporting frame cannot reduce the stress response of the slender UHV composite BPS to the satisfactory level.

Therefore, the applicability of WRIs in the seismic performance upgrading of the BPS is studied numerically. The modified Bouc-Wen model can effectively and accurately describe the hysteresis curves of the WRI in the C-T direction. The increase in energy dissipation capacity is found to be the critical point in seismic response mitigation. Therefore, it is recommended to adopt a smaller stiffness WRI with a larger radius or an increased loop WRI with smaller radius to increase energy dissipation while fixing the rotational stiffness of the isolation. Accordingly, a three-step design procedure of the wire rope isolation is proposed. The smaller stiffness and increased loop design of the isolation suggest an 8-loop WR28 isolator with a radius of 855 mm and 24-loop WR28 isolator with a radius of 489 mm, respectively. As a result, the two isolations both increase the stress safety factor to over 2.19 and peak displacement to below 0.7 m under seismic or wind loads. Hence, the application of wire rope isolation can be extended to UHV composite BPS with a very low natural frequency, but conductors with enough redundancy should be used in practice.

References

ABAQUS/Standard, Analysis User′s Manual, Dassault Systemes Simulia Corp. Providence, RI.

Alessandri S, Giannini R, Paolacci F and Malena M (2015), "Seismic Retrofitting of an HV Circuit Breaker Using Base Isolation with Wire Ropes. Part 1: Preliminary Tests and Analyses," *Engineering Structures*, **98**: 251–262.

Alessandri S, Giannini R, Paolacci F and Malena M (2015), "Seismic Retrofitting of an HV Circuit Breaker Using Base Isolation with Wire Ropes. Part 2: Shaking-Table Test Validation," *Engineering Structures*, **98**: 263–274.

Bai W, Dai JW, Zhou HM, Yang YQ and Ning XQ (2017), "Experimental and Analytical Studies on Multiple Tuned Mass Dampers for Seismic Protection of Porcelain Electrical Equipment," *Earthquake Engineering and Engineering Vibration*, **16**(4): 803–813.

Beheshti-Aval SB, Kouhestani HS and Mottaghi L (2017), "Effectiveness of Two Conventional Methods for Seismic Retrofit of Steel and RC Moment Resisting Frames Based on Damage Control Criteria," *Earthquake Engineering and Engineering Vibration*, **16**(3): 537–555.

Bhagat S and Wijeyewickrema AC (2017), "Seismic Response Evaluation of Base-Isolated Reinforced Concrete Buildings Under Bidirectional Excitation," *Earthquake Engineering and Engineering Vibration*, **16**(2): 365–382.

Cheng YF, Li S, Lu ZC and Liu ZL (2018), "Seismic Risk Mitigation of Cylindrical Electrical Equipment with a Novel Isolation Device," *Soil Dynamics & Earthquake Engineering*, **111**: 41–52.

Demetriades GF, Constantinou MC and Reinhorn AM (1993), "Study of Wire Rope Systems for Seismic Protection of Equipment in Buildings," *Engineering Structures*, **15**(5): 321–334.

Epackachi S, Dolatshahi KM, Oliveto ND and Reinhorn AM (2015), "Mechanical Behavior of Electrical Hollow Composite Post Insulators: Experimental and Analytical Study," *Engineering Structures*, **93**: 129–141.

Filiatrault A and Matt H (2006), "Seismic Response of High Voltage Electrical Transformer–Bushing Systems," *Journal of Structural Engineering*, **132**(2): 287–295.

GB 50260 (2013), *Code for Seismic Design of Electrical Installation*, Ministry of Housing and Urban-Rural Development of the People′s Republic of China, Beijing. (in Chinese)

Gökçe T, Orakdöğen E and Yüksel E (2017), "Seismic Protection of High Voltage Bushings by Using Polyuretan Springs," *Processing of the 13th World Conference on Earthquake Engineering*, Santiago, Chile.

He C, Xie Q, Yang ZY and Xue ST (2019), "Seismic Performance Evaluation and Improvement of Ultra-High Voltage Wall Bushing-Valve Hall System," *Journal of Constructional Steel Research*, **154**: 123–133.

He QQ, Yang ZY, Xie Q, Lu YX, Zhuo R, Hu R and Sun BX (2018), "Seismic Responses and Seismic Resistance Measure of ±800 kV Direct Current Bypass Switch," *High Voltage Apparatus*, **54**(2): 225–230. (in Chinese)

ITT Enidine. https://www.enidine.com/en-US/Products/WireRopeIsolator/.

Khanmohammadi M and Mohsenzadeh V (2018), "Effects of Foundation Rocking and Uplifting on Displacement Amplification Factor," *Earthquake Engineering and Engineering Vibration*, **17**(3): 511–525.

Koliou M, Filiatrault A and Reinhorn AM (2013), "Seismic Response of High-Voltage Transformer-Bushing Systems Incorporating Flexural Stiffeners I: Numerical Study," *Earthquake Spectra*, **29**(4): 1335–1352.

Koliou M, Filiatrault A and Reinhorn AM (2013), "Seismic Response of High-Voltage Transformer-Bushing Systems Incorporating Flexural Stiffeners II Experimental Study," *Earthquake Spectra*, **29**(4): 1353–1367.

Lee CL, Wang YP and Cai MY (2018), "An Experimental Study of In-Plane Arch-Shaped Dampers," *Earthquake Engineering and Engineering Vibration*, **17**(4): 849–867.

Li S, Tsang HH, Cheng YF and Lu ZC (2017a), "Effects of Sheds and Cemented Joints on Seismic Modelling of Cylindrical Porcelain Electrical Equipment in Substations," *Earthquakes and Structures*, **12**(1): 55–65.

Li S, Tsang HH, Cheng YF and Lu ZC (2017b), "Considering Seismic Interaction Effects in Designing Steel Supporting Structure for Surge Arrester," *Journal*

of Constructional Steel Research, **132**: 151–163.

Li S, Tsang HH, Cheng YF and Lu ZC (2018), "Seismic Testing and Modeling of Cylindrical Electrical Equipment with GFRP Composite Insulators," *Composite Structures*, **194**: 454–467.

Liang Chao, Zhang Jinliang, Lian Jijian, Liu Fang and Li Xinyao (2017), "Probabilistic Analysis for the Response of Nonlinear Base Isolation System Under the Ground Excitation Induced by High Dam Flood Discharge," *Earthquake Engineering and Engineering Vibration*, **16**(4): 841–857.

Moustafa MA and Mosalam KM (2016), "Structural Performance of Porcelain and Polymer Post Insulators in High Voltage Electrical Switches," *Journal of Performance of Constructed Facilities*, **30**(5): 04016002.

Ni YQ, Ko JM, Wong CW and Zhang S (1999), "Modelling and Identification of a Wire-Cable Vibration Isolator via a Cyclic Loading Test," *Proceedings of the Institution of Mechanical Engineers, Part I: Journal of Systems and Control Engineering*, **213**(3): 163–172.

Paolacci F and Giannini R (2008), "Study of the Effectiveness of Steel Cable Dampers for the Seismic Protection of Electrical Equipment," *Proceedings of 14th World Conference on Earthquake Engineering*, Beijing, China.

Paolacci F, Giannini R, Alessandri S and De Felice G (2014), "Seismic Vulnerability Assessment of a High Voltage Disconnect Switch," *Soil Dynamics & Earthquake Engineering*, **67**: 198–207.

Prost C and Partyka J (2016), "Using Wire Rope Isolators for Seismic Protection," *Sound & Vibration*, 8–11.

Puff M, Kopanoudis A, Seck AV and Ruan S (2015), "Introduction of an Innovative Base Isolation System for Seismic Protection of HV Components Based on a Combination of Wire Ropes and Viscous Dampers," *Proceeding of 10th International Conference on Earthquake Resistant Engineering Structures*, Opatija, Croatia.

Riley M, Stark C, Kempner L, Kempner Jr L and Mueller W (2006), "Seismic Retrofit Using Spring Damper Devices on High-Voltage Equipment Stands," *Earthquake Spectra*, **22**(3): 733–753.

Roh H, Oliveto ND and Reinhorn AM (2012), "Experimental Test and Modeling of Hollow-Core Composite Insulators," *Nonlinear Dynamics*, **69**(4): 1651–1663.

Schwanen W (2004), "Modelling and Identification of the Dynamic Behavior of a Wire Rope Spring," *Master Thesis*, Technische Universiteit Eindhoven, Netherlands, Report number: DCT-2004/28, 2004.

Tinker ML and Cutchins MA (1992), "Damping Phenomena in a Wire Rope Vibration Isolation System," *Journal of Sound and Vibration*, **157**(1): 7–18.

Vaiana N, Spizzuoco M and Serino G (2017), "Wire Rope Isolators for Seismically Base-Isolated Lightweight Structures: Experimental Characterization and Mathematical Modeling," *Engineering Structures*, **140**: 498–514.

Vaiana N, Sessa S, Marmo F and Rosati L (2018), "A Class of Uniaxial Phenomenological Models for Simulating Hysteretic Phenomena in Rate-Independent Mechanical Systems and Materials," *Nonlinear Dynamics*, **93**(3): 1647–1669.

Vaiana N, Sessa S, Marmo F and Rosati L (2019a), "An Accurate and Computationally Efficient Uniaxial Phenomenological Model for Steel and Fiber Reinforced Elastomeric Bearings," *Composite Structures*, **211**: 196–212.

Vaiana N, Sessa S, Marmo F and Rosati L (2019b), "Nonlinear Dynamic Analysis of Hysteretic Mechanical Systems by Combining a Novel Rate-Independent Model and an Explicit Time Integration Method," *Nonlinear Dynamics*, 1–23.

Wang CF, Zhao JK, Zhu L, and Bao YJ (2016), "Effects of Vertical Excitation on the Seismic Performance of a Seismically Isolated Bridge with Sliding Friction Bearings," *Earthquake Engineering and Engineering Vibration*, **15**(1): 187–196.

Wang HX., Gong XS, Pan F and Dang XJ (2015), "Experimental Investigations on the Dynamic Behaviour of O-Type Wire-Cable Vibration Isolators," *Shock and Vibration*, **2015**: 1–12.

Whittaker AS, Fenves GL and Gilani ASJ (2007), "Seismic Evaluation and Analysis of High-Voltage Substation Disconnect Switches," *Engineering Structures*, **29**(12): 3538–3549.

Xia JY, Ning XL, Tan P, Hao HX and Chen GP (2015), "Impact of the Equivalent Center of Mass Separating from the Sliding Surface on the Isolation Performance of Friction Pendulum Bearings," *Earthquake Engineering and Engineering Vibration*, **14**(4): 695–702.

Xie Q and Zhu RY (2011), "Earth, Wind, and Ice," *Journal of IEEE Power Energy Magazine*, **9**(2): 28–36.

Xie Q, Yang ZY, He C and Xue ST (2019), "Seismic Performance Improvement of a Slender Composite Ultra-High Voltage Bypass Switch Using Assembled Base Isolation," *Engineering Structures*, **194**: 320–333.

Xue SD, Shan MY, Li XY, Liang SZ, Huang FY and Liu Yi (2019), "Shaking Table Test and Numerical Simulation of an Isolated Cylindrical Latticed Shell Under Multiple-Support Excitations," *Earthquake Engineering and Engineering Vibration*, **18**(3): 611–630.

Yang ZY, Xie Q, Zhou Y and Mosalam KM (2018), "Seismic Performance and Restraint System of Suspended 800 kV Thyristor Valve," *Engineering Structures*, **169**: 179–187.

Zareei SA, Hosseini M and Ghafory-Ashtiany M (2017), "Evaluation of Power Substation Equipment Seismic Vulnerability by Multivariate Fragility Analysis: A Case Study on a 420 kV Circuit Breaker," *Soil Dynamics &*

Earthquake Engineering, **92**: 79–94.

Zhao GF, Ma YH, Li YM, Luo JR and Du C (2017), "Development of a Modified Mooney-Rivlin Constitutive Model for Rubber to Investigate the Effects of Aging and Marine Corrosion on Seismic Isolated Bearings," *Earthquake Engineering and Engineering Vibration*, **16**(4): 815–826. https://doi.org/10.1007/s11803-017-0417-6

Zhou FL and Tan P (2018), "Recent Progress and Application on Seismic Isolation Energy Dissipation and Control for Structures in China," *Earthquake Engineering and Engineering Vibration*, **17**(1): 19–27.

Zhou XL, Yi J, Song RH, Yang XY, Li Y and Tang HY (2010), "An Overview of Power Transmission Systems in China," *Energy*, **35**(11): 4302–4312.